LETTER

Formation of metal vacancy arrays in coalesced WS$_2$ monolayer films

View the article online for updates and enhancements.

2D Materials

Formation of metal vacancy arrays in coalesced WS$_2$ monolayer films

Danielle Reifsnyder Hickey[1] , Dundar E Yilmaz[2], Mikhail Chubarov[3] , Saiphaneendra Bachu[1],
Tanushree H Choudhury[3], Leixin Miao[1], Chenhao Qian[1], Joan M Redwing[1,3] , Adri C T van Duin[2]
and Nasim Alem[1,*]

[1] Department of Materials Science and Engineering, The Pennsylvania State University, University Park, PA 16802,
   United States of America
[2] Department of Mechanical Engineering, The Pennsylvania State University, University Park, PA 16802, United States of America
[3] 2-Dimensional Crystal Consortium (2DCC), Materials Research Institute, The Pennsylvania State University, University Park, PA 16802,
   United States of America
*   Author to whom any correspondence should be addressed

E-mail: nua10@psu.edu

Abstract

Defects have a profound impact on the electronic and physical properties of crystals. For two-dimensional (2D) materials, many intrinsic point defects have been reported, but much remains to be understood about their origin. Using scanning transmission electron microscopy imaging, this study discovers various linear arrays of W-vacancy defects that are explained in the context of the crystal growth of coalesced, monolayer WS$_2$. Atomistic-scale simulations show that vacancy arrays can result from steric hindrance of bulky gas-phase precursors at narrowly separated growth edges, and that increasing the edge separation leads to various intact and defective growth modes, which are driven by competition between the catalytic effects of the sapphire substrate and neighboring growth edge. Therefore, we hypothesize that the arrays result from combined growth modes, which directly result from film coalescence. The connections drawn here will guide future synthetic and processing strategies to harness the engineering potential of defects in 2D monolayers.

1. Introduction

Atomic-scale defects such as vacancies can dramatically affect the physical and electronic properties in atomically thin, two-dimensional (2D) transition metal dichalcogenide (TMD) monolayers. For example, vacancies can alter a TMD material's absorption [1] and photoluminescence [2], Fermi level [1], electron mobility [2], charge-carrier type [3] and dynamics [4], spin polarization [1], elastic modulus, and tensile strength [5]. Additionally, *ab initio* quantum transport simulations have predicted that the position of atomic defects in a monolayer TMD affects both the performance and reliability of tunneling field-effect transistors (TFETs) [6]. These properties have important implications for TMD-based electronic and optoelectronic devices, and therefore, it is imperative to identify vacancy

structures and to relate their formation to crystal growth.

Many studies on TMD defects have focused on chalcogen vacancies, especially those created by external stimuli such as electron or ion beams [7–10], or due to nonequilibrium growth methods such as laser-evaporation synthesis [3]. Additionally, methods have been developed for the post-synthesis modification of TMDs, such as introducing chemically sourced sulfur atoms to fill chalcogen vacancies in sulfides [11] and the introduction of excess metal atoms, which leads to local phase transitions [12]. However, as bottom-up synthesis methods such as chemical vapor deposition (CVD) and molecular beam epitaxy (MBE) improve film quality [13–22], the vacancies resulting from growth become increasingly relevant. Metal vacancies, specifically, can affect properties in numerous ways. For example,

single-W-vacancy point defects in CVD-grown films of WSe$_2$ have caused p-type doping of WSe$_2$ monolayers and dominated the low-temperature optical spectra as localized excitons [23]. Such localized emission can create single quantum emitters, which are the basis for quantum information processing. Additionally, the mid-band-gap states created by a single-M vacancy in MX$_2$ (M = Mo,W; X = S, Se) reduce the effective length of the tunneling transition region in TFETs, enhancing the on-state tunneling current [24]. Further, M vacancies produce inter-valley scattering in the conduction band of TMDs, which reduces valley lifetimes and hinders application of TMDs in the emerging field of valleytronics [25]. Beyond observing the properties of intrinsic defects, decorating W-vacancy sites in WSe$_2$ with K atoms has also enabled engineering of the defect state wavefunction, relevant to magnetic and spin-based applications [26].

In this study, we provide direct visualization and an in-depth understanding of the formation of intrinsic metal vacancies arising from the metal–organic CVD (MOCVD) crystal growth of WS$_2$ monolayer films. Utilizing scanning transmission electron microscopy (STEM) imaging, we discover various morphologies of W-vacancy arrays, and we harness molecular dynamics (MD) simulations to elucidate the mechanisms by which defect arrays form. To provide an accurate description of the chemistry and dynamics of the system, we apply the widely used ReaxFF reactive force field [27] that was developed for hydrocarbons [28] and then later applied to a wide range of materials, including ceramics [29], explosives [30], metal-organic frameworks [31], ferroelectric materials [32, 33], polymeric systems [34–36], and 2D materials [37–39]. When properly trained, ReaxFF provides an accuracy approaching that of density functional theory-based methods with a computational performance that is over six orders of magnitude faster, enabling simulations of large, realistic systems [40]. Moreover, coupled with more advanced techniques, such as meta-dynamics [41], replica exchange [42], and bond restraints, ReaxFF can also provide insights into rare events, including reaction barriers and binding energies on a size scale directly comparable to that of experiment.

Through atomic-resolution observation using annular dark-field (ADF-) STEM, we observe arrays of W vacancies and vacancy clusters in straight and faceted lines. These features are unexpected in the epitaxially grown monolayer films and are not accompanied by local distortions or lattice offsets around the defect sites. In contrast to isolated vacancies that have often been observed in TMD monolayers, the vacancy clustering presented here arises from crystal growth and provides an opportunity to determine a direct link to the film growth mechanism. Through the combination of experimental observations and

MD simulation, we propose the formation mechanism for W vacancies and vacancy clusters by simulating the incorporation of precursors from the gas phase and the catalytic effects of the sapphire substrate and the adjacent WS$_2$ edge.

2. Results and discussion

The controlled growth of single-crystalline, monolayer films of TMDs poses a major challenge, even using precise, bottom-up methods such as MOCVD and MBE. To produce a perfect film, the growth temperatures and reactivities of precursors must be well-matched, the substrate must provide effective epitaxial templating of a film with a single orientation, and conditions must promote monolayer growth while suppressing multilayer nucleation. However, in reality, many factors can lead to incomplete, misoriented, or thicker films. Recently, the MOCVD growth of WS$_2$ has achieved high-quality, unidirectional monolayer films via a three-step method that allows for distinct nucleation, ripening, and monolayer lateral growth steps [20]. Yet, despite the large-scale homogeneity of the films, we observe W-vacancy arrays locally in these films. These vacancy arrays, such as the continuous array presented in figures 1(a)–(c), cause negligible distortion to the host lattice. Figures 1(a) and (b) show a coherent 2H WS$_2$ lattice containing a row of missing W atoms with the surrounding S lattice sites occupied. Visual inspection of the ADF-STEM image (figure 1(b)) and direct measurement of the distances between the W atoms in the image (figure 1(c)), show that the vacancy array negligibly perturbs the nearby lattice structure. The W–W atom distance map in figure 1(c) shows the deviation in picometers from the theoretical value [43] of the metal–metal distance. No systematic distortion of the lattice is observed around the array of missing W atoms, and no significant structural relaxation of metal atom positions occurs. We also observe that the neighboring W atoms are fully terminated by sulfur atoms, in the areas that the sulfur atoms are visible along these vacancy arrays. In addition to continuous arrays, atomic-resolution imaging shows that these films contain several other types of W-vacancy arrays, including aligned point defects of isolated, single-W vacancies (figure 1(d)) and linear arrays of multi-W-vacancy clusters (figure 1(e)). These defect arrays occur in films that previously have been confirmed to be predominantly monolayer and single-orientation [20, 21], consistent with the representative selected-area electron diffraction pattern (figure 1(f) inset) and corresponding bright-field (BF-) (figure 1(f)) and dark-field (DF-) (figure 1(g)) TEM images shown here. In these films, the uniformity in the BF-TEM image contrast (figure 1(f)) correlates with the monolayer thickness demonstrated by atomic force microscopy (AFM) [20] and ADF-STEM intensity linescans [21], and the DF-TEM image in
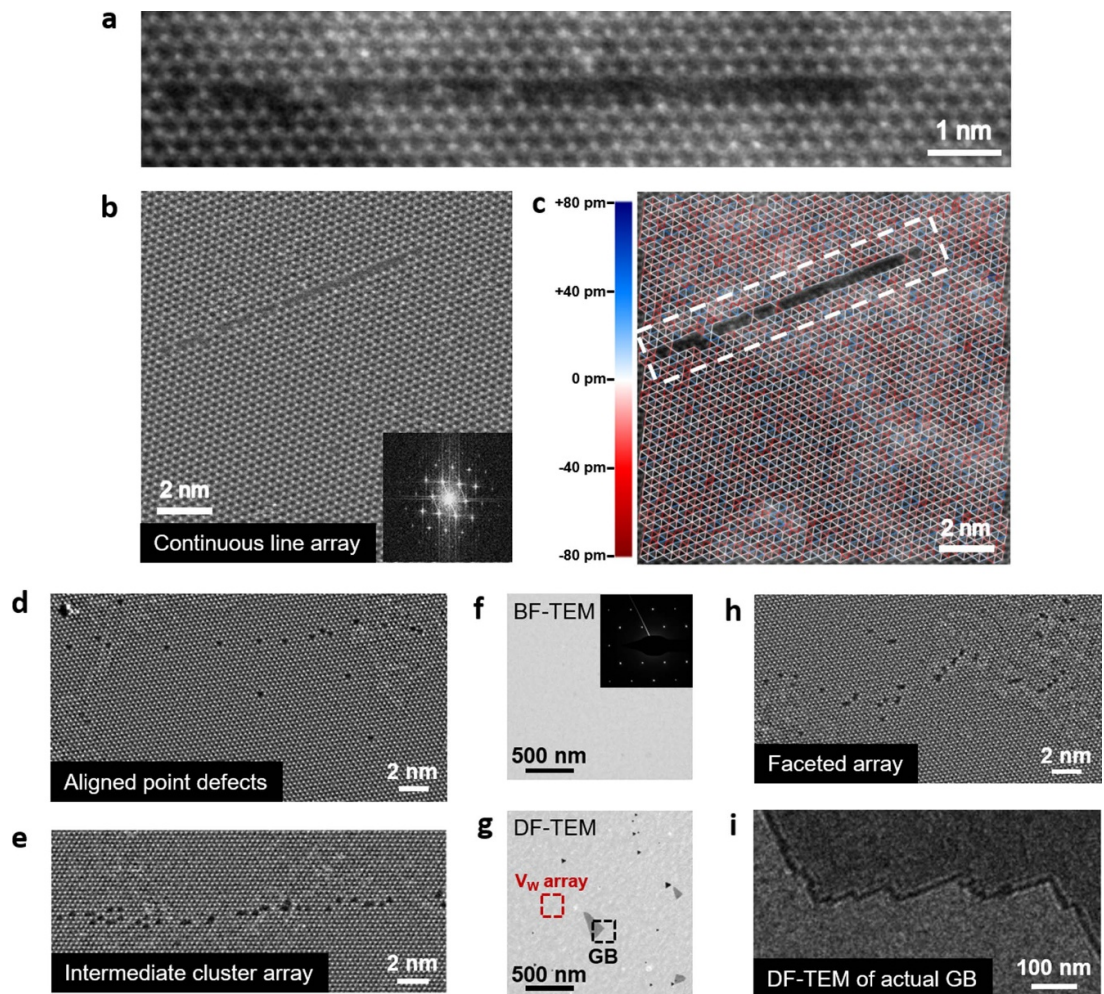
Figure 1. Types of W-vacancy arrays in WS$_2$ monolayer films. (a) ADF-STEM image of a continuous W-vacancy line and (b) the WS$_2$ lattice surrounding it (inset: FFT). (c) W–W atom distance map overlaid onto the region in (b), showing positive (blue) and negative (red) deviations from the theoretical W–W atom distance. (d), (e) ADF-STEM images of linear arrays of (d) isolated single-W vacancies with scatter and (e) single- and multiple-W-vacancy clusters. (f) BF-TEM image of a representative 2 μm^2 region from a WS$_2$ film (inset: SAED pattern) containing vacancy arrays and (g) the corresponding DF-TEM image. In (g), the dashed boxes indicate representative areas in which a W-vacancy array (maroon) and a grain boundary (black) are observed. (h) ADF-STEM image of a faceted W-vacancy array. (i) DF-TEM image of a representative actual GB with faceting geometry similar to that of the defect array in (h).

figure 1(g) shows the presence of only a few small defects (black triangles are holes in the film, and dark gray areas are regions with translational offset, as reported in [20, 21].). In the DF-TEM image in figure 1(g), grain boundaries exist at the interface between light and dark gray regions, such as that indicated by the dashed black box. In contrast, the vacancy arrays reported here occur in the single-contrast, nearly featureless region, such as that indicated by the dashed maroon box. As a result, DF-TEM imaging does not provide a map of their location, and they can instead only be located by atomic-resolution imaging. The type of DF-TEM contrast indicated by the maroon box comprises the majority of the film, which was grown by the coalescence of nuclei separated by <100 nm, as shown by AFM [20]. Therefore, the film was grown by stitching many small islands together. Because the W-vacancy defects occur as arrays instead of being randomly distributed throughout the film, it appears

that they are vestiges of the coalescence of the small initial grains that merged with the same orientation. It is expected that they are also distributed in the film no closer than the distance between coalescing islands, which is qualitatively consistent with atomic-resolution imaging. This is, however, difficult to statistically probe because of the difference in length scales and lack of large-scale defect features to act as fiducial markers during large-area imaging at atomic resolution.

Strikingly, however, not all of the W-vacancy defect arrays are linear (figure 1(h)), and the local morphology mimics that of the facets of grain boundaries also observed in these films, albeit on a much larger length scale (figure 1(i)). This unusual grain boundary morphology has previously been linked to relatively fast growth rates that favor kinetically driven faceting [21]. Regardless of the exact morphology of each type of W-vacancy array shown in figures 1(a)–(e) and (h), the arrays are not perfectly
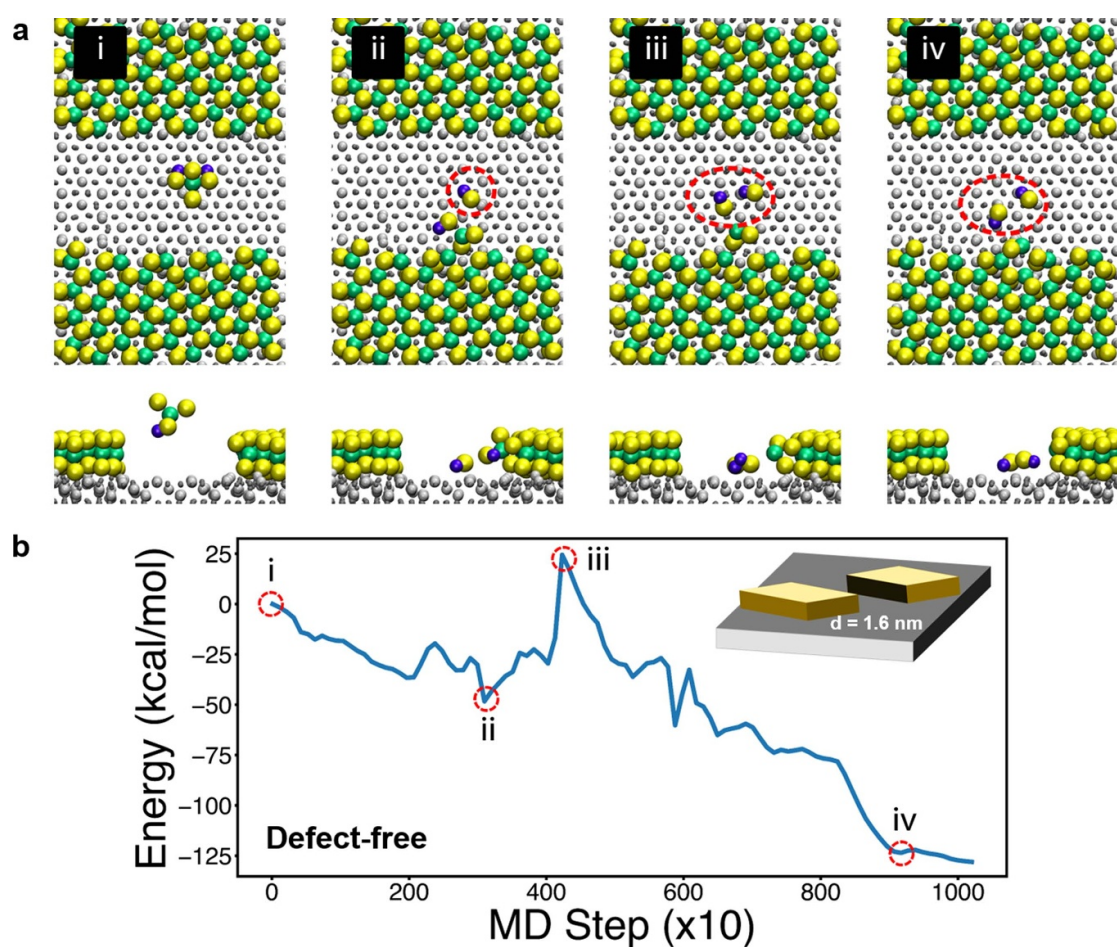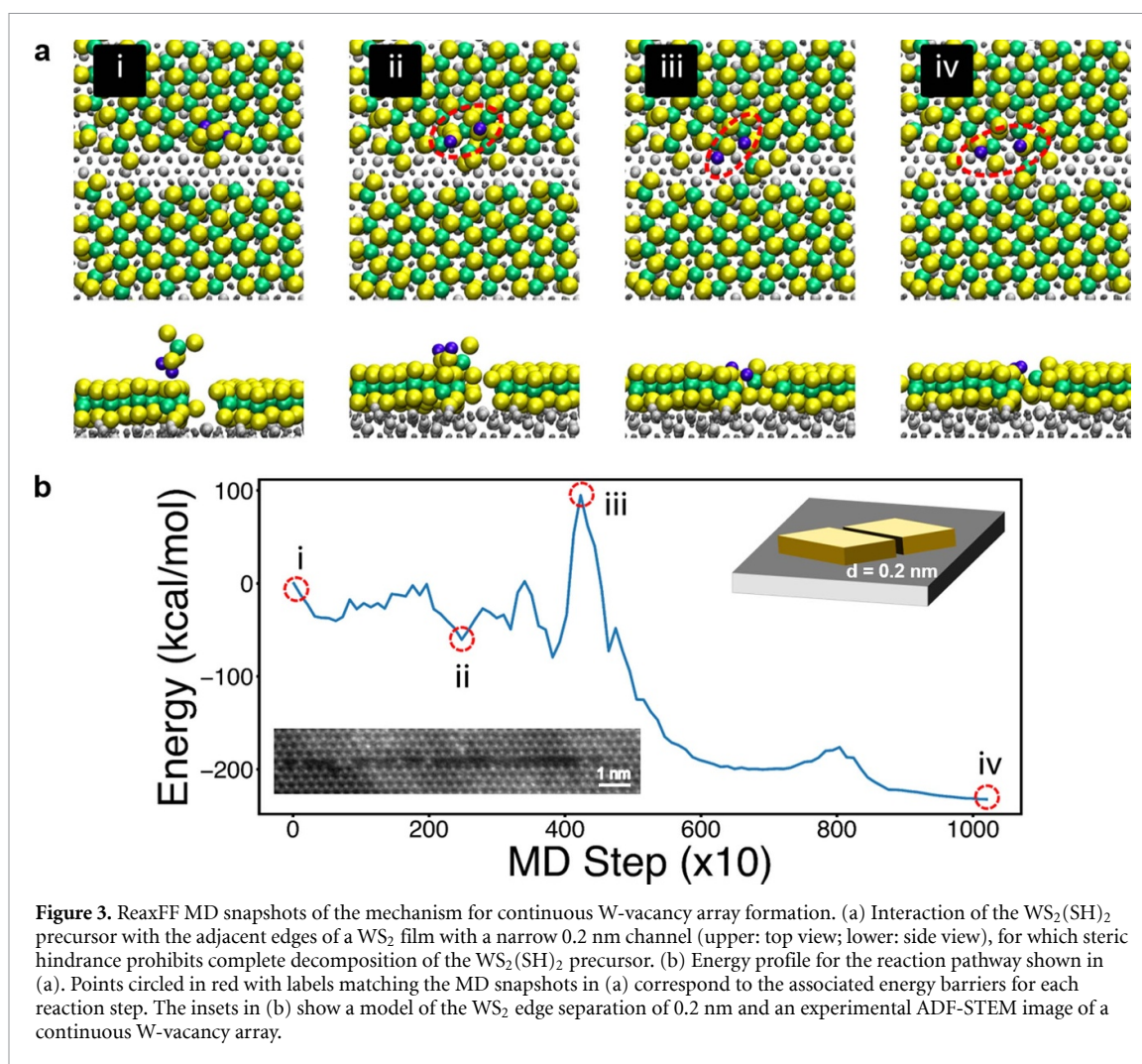
Figure 2. ReaxFF MD snapshots of the mechanism of WS$_2$ edge growth. (a) Reaction of the WS$_2$(SH)$_2$ precursor with the edge of a WS$_2$ monolayer film (upper: top view; lower: side view). WS$_2$(SH)$_2$ (i) approaches a channel between two WS$_2$ edges, (ii), (iii) interacts with the sapphire substrate, causing loss of the first (ii) and second (iii) –SH groups (circled in red), and (iv) leads to WS$_2$ edge growth by attachment of the remaining WS$_2$ unit. W = green, S = yellow, and H = blue. (b) Energy profile of the reaction pathway shown in (a). Points circled in red with labels matching the MD snapshots in (a) correspond to the associated energy barriers for each reaction step. The inset in (b) shows a model of the WS$_2$ edge separation of 1.6 nm.

linear and localized; in many cases, a minority of vacancies also exist scattered off the array, suggesting that their formation is not a perfectly controlled process.

To uncover the origin of these W-vacancy arrays, we performed ReaxFF MD simulations of the WS$_2$ edge growth process, using the W/S/H ReaxFF description that was developed via a strategy similar to the ReaxFF description for MoS$_2$ developed by Ostadhossein *et al* [37] and Yilmaz *et al* [38]. This W/S/H ReaxFF description was merged with the Hong *et al* [44]. ReaxFF Al/O/C/H parameters to enable simulations of WS$_2$ on Al$_2$O$_3$ surfaces. These simulations provide insights into the likely reaction pathway and evidence for energy barriers that hinder WS$_2$ monolayer film growth and coalescence. During growth, the gaseous reactants W(CO)$_6$, H$_2$S, and H$_2$ flow into the MOCVD chamber and deposit a monolayer WS$_2$ film onto a *c*-axis-oriented sapphire ((0001) α-Al$_2$O$_3$) substrate (see Supplementary information). Based on previous simulations considering multiple reaction pathways [45],

the film growth is expected to occur primarily by the decomposition of the intermediate W-S-containing precursor species WS$_2$(SH)$_2$ or a similar relatively large gas-phase species like WS$_3$. For the growth of WS$_2$ films, the sapphire surface can play a catalytic role, lowering the energy barrier to dissociate –SH groups. By sequentially losing two –SH groups, the precursor decomposes into a WS$_2$ unit that has the correct stoichiometry for addition onto the film's growth edge. Here, we modeled two adjacent WS$_2$ growth edges separated by a parallel channel, and bond restraints were applied to drive the set of chemical reactions that leads to the loss of –SH groups from W(SH)$_2$S$_2$ and bonding to the growth edge (see Supplementary information). This additional energy term drives the atoms together to accelerate the chemical reactions that form the targeted bonds in the system. To measure reaction barriers, the total energy of the system was recorded, excluding the contribution from the bond restraint terms.

Our experimental observations show that the vacancy arrays can be observed along multiple edge

Figure 3. ReaxFF MD snapshots of the mechanism for continuous W-vacancy array formation. (a) Interaction of the $WS_2(SH)_2$ precursor with the adjacent edges of a WS_2 film with a narrow 0.2 nm channel (upper: top view; lower: side view), for which steric hindrance prohibits complete decomposition of the $WS_2(SH)_2$ precursor. (b) Energy profile for the reaction pathway shown in (a). Points circled in red with labels matching the MD snapshots in (a) correspond to the associated energy barriers for each reaction step. The insets in (b) show a model of the WS_2 edge separation of 0.2 nm and an experimental ADF-STEM image of a continuous W-vacancy array.

types. Therefore, in addition to the edge configuration, other parameters, such as the substrate surface and the gap between the two grains, should also play an important role in the growth transition dynamics of the grains and the formation of the vacancy array. We have simulated the transition dynamics of growth both along the armchair (figures 2, 3 and 5) and zigzag (figure S1 (is available online at https://stacks.iop.org/2DM/08/011003/mmedia)) edges to show that the growth mechanism shows the same trend for both cases.

Figures 2(a) and (b) present the proposed reaction pathway for the precursor $WS_2(SH)_2$ to (i) approach the sapphire substrate, (ii and iii) sequentially lose its two –SH groups as they bind to the substrate in the channel, and then (iv) result in the addition of a WS_2 unit to the growing WS_2 monolayer's edge. Figure 2(a) shows models of the WS_2-sapphire system that detail the reaction pathway, with the corresponding plot of the reaction energy shown in figure 2(b). In this case, the channel distance is large (1.6 nm), which provides sufficient area for the $WS_2(SH)_2$ precursor to approach the surface, interact with the sapphire, and bond to the WS_2 growth edge as expected. Four bond restraints were imposed: two

bond restraints between the S atoms of the precursor and a W atom on the growth edge, and two bond restraints between the S atoms in the –SH groups and the surface Al atoms. These bond restraints drive the precursor to the growth edge and extract the –SH groups, respectively. The reaction barrier for removing the first –SH group is $\sim$25 kcal mol^{-1}. This strengthens the remaining W–S bonds in the precursor, and therefore, the energy barrier for breaking the second –SH group increases to $\sim$75 kcal mol^{-1}. After the –SH groups are removed from the precursor, the remaining bond restraints continue to drive the precursor to the growth edge. At this point, because the precursor has lost its two –SH groups and now contains only two S atoms and dangling bonds, the reaction proceeds downhill, releasing energy as the WS_2 unit bonds to the growth edge. Overall, the reaction is exothermic with a net energy release of $\sim$125 kcal mol^{-1} (figure 2(b)), and with the largest energy barrier of $\sim$75 kcal mol^{-1} occurring at the loss of the second –SH group in step (iii).

In figures 2(a) and (b), no defects form because the channel between the WS_2 edges is large enough that the precursor/substrate interaction is unencumbered. However, continuous W-vacancy line
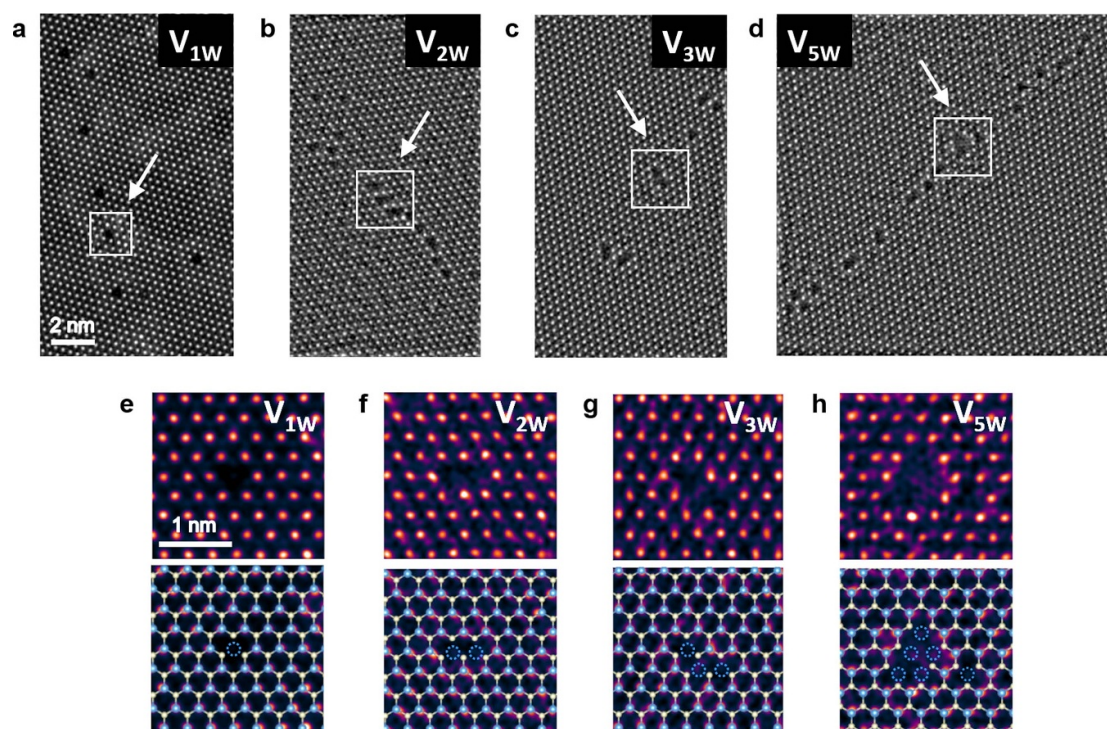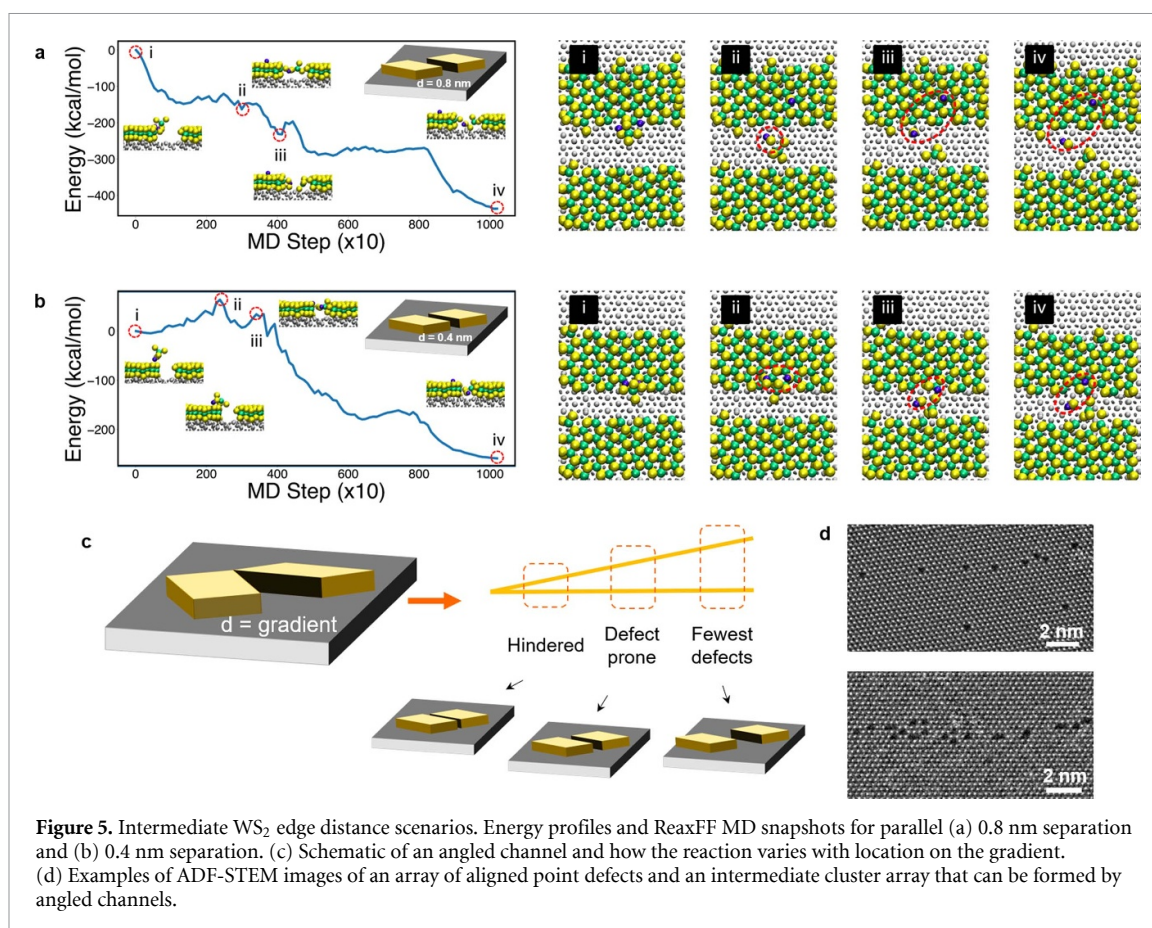
Figure 4. Types of W-vacancy clusters and arrays observed in WS$_2$ monolayer films. (a)–(d) ADF-STEM images of vacancy arrays that include various vacancy clusters. White boxes and arrows indicate examples of vacancy clusters. (e)–(h) ADF-STEM images with ball-and-stick atomic models overlaid for (e) single-, (f) double-, (g) triple-, and (h) quintuple-W vacancy clusters (for the models, W = blue and S = yellow).

arrays (figures 1(a)–(c)) can be explained by a scenario in which the two WS$_2$ edges have very narrow separation, i.e. during the final stage of coalescence of two parallel edges. In this case, the narrow gap inhibits decomposition of the WS$_2$(SH)$_2$ precursor because the growing film blocks access to the catalytic Al$_2$O$_3$ substrate surface. Figures 3(a), (b) show the simulated reaction mechanism and energy profile for a narrow (0.2 nm) channel. This narrow separation produces a significant energy barrier of >100 kcal mol^{-1}. In this case, the channel is not large enough for the –SH groups to interact with the substrate. Thus, when the precursor approaches the growth edge, the –SH groups directly interact with the second edge, which abstracts one of the H atoms, and then steric hindrance prevents further decomposition of the bulky WS$_3$(SH) molecule into the WS$_2$ unit necessary for defect-free growth. Although the 0.2 nm channel creates an overall exothermic reaction (∼200 kcal mol^{-1}), the energy barrier in step (iii) is very large, making this reaction pathway kinetically unfavorable under the conditions studied. As a result, such narrow separation of the two WS$_2$ edges can create a continuous array of W vacancies, such as that in figure 1(a).

Regarding clustering of W vacancies into arrays, the extreme cases are a continuous W-vacancy array (figures 1(a)–(c)) and an array of aligned point defects (figure 1(d)). However, arrays of intermediately sized W-vacancy clusters also exist. For these, arrays of vacancy clusters are aligned but imperfectly. Figures 4(a)–(d) presents ADF-STEM images of several vacancy cluster arrays. These arrays include clusters of different sizes, such as the single-, double-, triple-, and quintuple-W vacancy clusters shown with overlaid ball-and-stick atomic models in figures 4(e)–(h). These vacancy cluster building blocks organize into extended linear structures that are reminiscent of grain boundaries, but without any offset or misorientation of adjacent grains that would exist at an actual grain boundary. Instead, the vacancy clusters represent defects associated with the coalescence of aligned grains. However, in certain regions, it appears that the growth process encounters an obstacle to the perfect coalescence of islands, leaving behind a row of vacant metal sites.

What happens to the vacancy formation energetics at an intermediate gap size? To answer this question and gain insights into how W-vacancy arrays occur, we tuned the gap between the WS$_2$ edges in our ReaxFF simulations. For example, reducing the channel distance to 0.8 nm or 0.4 nm separation (figure 5) from 1.6 nm accelerates the reaction due to the proximity of the second WS$_2$ edge. For 0.8 nm (figure 5(a)), as the precursor passes the second edge, an S atom at the second edge captures one H atom from an –SH group of the precursor and pulls the other –SH group with an energy release of ∼150 kcal mol^{-1} (step ii). Due to interaction with the second growth edge and the bond restraints

Figure 5. Intermediate WS$_2$ edge distance scenarios. Energy profiles and ReaxFF MD snapshots for parallel (a) 0.8 nm separation and (b) 0.4 nm separation. (c) Schematic of an angled channel and how the reaction varies with location on the gradient. (d) Examples of ADF-STEM images of an array of aligned point defects and an intermediate cluster array that can be formed by angled channels.

driving the remaining –SH group down to the substrate, the reaction barrier to remove the second –SH group from the precursor vanishes. Instead, this reaction step becomes significantly exothermic (step iii). At this point, one H and one –SH group have been removed from the precursor, leaving three S atoms and a W atom. After a relatively small barrier of ∼40 kcal mol^{-1}, WS$_3$ is driven to the growth edge, with an overall energy release >400 kcal mol^{-1}. The strong exothermicity of the system throughout the reaction suggests that having a second growth edge near the system accelerates growth. Further narrowing the gap to 0.4 nm, the reaction proceeds similarly (figure 5(b)), but the effect is weaker due to the decreased distance to the second WS$_2$ edge. For this case, the reaction barriers for steps (ii) and (iii) are small (∼25–50 kcal mol^{-1}) compared to those for the widest (1.6 nm) and narrowest (0.2 nm) separation distances, and the overall reaction is exothermic, releasing ∼200 kcal mol^{-1} less than for 0.8 nm separation. However, in both cases, a WS$_3$ unit bonds to the WS$_2$ edge instead of a WS$_2$ unit, which can result in point or cluster W-vacancy defects at the interface due to the off-stoichiometry and steric hindrance.

Experimentally, we observe a spectrum of W-vacancy array types (figures 1 and 4), ranging from arrays of isolated single-W point vacancies, to aligned multi-W-vacancy clusters, to continuous arrays of W

vacancies. To account for the morphology differences, we apply the ReaxFF insights gained for various WS$_2$ edge separation distances (figures 2, 3, and 5) and consider a more complicated case. Here (figure 5(c)), the two grains are separated by an angled gap, rather than the idealized parallel channels modeled. This angled gap acts as a composite of the narrow (0.2 nm), intermediate (0.4 nm or 0.8 nm), and wide (1.6 nm) parallel channels. Therefore, neighboring regions of the channel react via different mechanisms and at dissimilar rates. The tip of the angle is sterically hindered, the intermediate gap region reacts easily but with defects, and the wide gap region proceeds with the fewest defects. Thus, depending on the angle between the growth fronts of the two WS$_2$ grains, arrays of either isolated W vacancies or W-vacancy clusters form. In every case observed, however, the result is a coherently stitched WS$_2$ film in which W-vacancy arrays are the only vestiges of the locations of coalescence.

3. Conclusion

In conclusion, we have discovered metal-vacancy arrays resulting from the growth of coalesced WS$_2$ monolayer films and explained their formation, opening up a route to engineer natively formed defects. Using atomic-resolution imaging and ReaxFF MD simulations, we have analyzed the W-vacancy

array morphologies and determined their underlying crystal growth mechanisms. From our observations of W-vacancy array morphologies and the calculated energy barriers, we show that precursor decomposition occurs due to the catalytic effects of both the sapphire substrate and the adjacent WS$_2$ edge. Additionally, we show that the separation distance of the coalescing WS$_2$ edges profoundly affects the growth mechanism, causing the film to incorporate defects. This understanding is key to engineering vacancy formation and annihilation during film growth and processing, for instance by tuning post-growth annealing or providing less sterically hindered metal precursors during the final stages of growth to ensure complete coalescence. Further, this study provides a route to create rationally patterned heterostructures via incorporation of heteroatoms at predetermined growth stages or else to alter the optical, electronic, or magnetic properties via post-growth decoration of W-vacancy sites with other species.

4. Methods

4.1. WS$_2$ film growth
Monolayer WS$_2$ films were grown on two-inch c-plane sapphire substrates in a horizontal, cold-wall, gas-source CVD reactor. An inductively coupled graphite susceptor was used for heating the substrate. The precursors tungsten hexacarbonyl (W(CO)$_6$) and hydrogen sulfide (H$_2$S) (tungsten and sulfur precursors, respectively) were introduced separately to the heated zone, and hydrogen (H$_2$) carrier gas was used. The growth was achieved via a multistep process at 850 °C and 1000 °C with a constant reactor pressure of 50 Torr and H$_2$S partial pressure of 4.4 Torr. The W(CO)$_6$ partial pressure was modulated: it was 14×10^{-7} Torr during nucleation and 7×10^{-7} Torr during growth, and it bypassed the reactor during the ripening step. The growth method is described in greater detail in Chubarov *et al* [20].

4.2. Transfer of WS$_2$ films onto TEM substrates
An NaOH-based transfer method was used to delaminate the WS$_2$ films from the sapphire growth substrates and transfer them onto Quantifoil 3 mm Cu TEM grids. The final films were freestanding across 2 μm-diameter holes in the carbon Quantifoil substrate. WS$_2$ films on sapphire were spin-coated with poly(methyl methacrylate) (PMMA), after which a razor blade was used to scratch away portions at the edges. A 1M aqueous NaOH solution was heated on a hotplate to 90 °C, and the sapphire/WS$_2$/PMMA was placed into the solution until the film started to detach. Next, the substrate was dipped in and out of the solution until the film floated freely on the liquid's surface. A glass slide was used to scoop up the floating film, which was then transferred sequentially into four water baths for rinsing. Finally, the film was scooped out using the

TEM grid, which was heated on a hotplate at 70 °C for 10 min so that the film stuck firmly to the grid. The prepared grid was placed into an acetone bath to soak for 1 h, after which it was rinsed in a methanol bath for 10 min. The grid was dried overnight under vacuum.

4.3. TEM analysis
An FEI Titan [3] G2 S/TEM was employed to collect ADF-STEM images at an accelerating voltage of 80 kV with a probe convergence angle of 30 mrad and probe current of 70 pA. ADF-STEM images were processed using either a two-pixel Gaussian blur or, when hydrocarbon-based residue remaining from sample transfer was present on or near features of interest, using bandpass filtering in ImageJ. For example, in ImageJ, values could be set to 'filter large structures down to' = 40 pixels and 'filter small structures up to' = 3 pixels. This contamination is a common artifact from PMMA-based sample transfer. An FEI Talos F200X TEM was used to collect selected-area electron diffraction patterns and BF- images, as well as DF-TEM images, which were acquired using a 10 μm objective aperture around the (10$\bar{1}$0) diffraction spot.

4.4. Theoretical modeling of W-vacancy arrays in WS$_2$
The Large-scale Atomic/Molecular Massively Parallel Simulator [46] with ReaxFF implementation [47] was used for MD simulations. The simulation box dimensions were set to $4.75 \times 5.76 \times 3.5$ nm in the *x*, *y*, and *z* dimensions, respectively. A sapphire substrate that contains 4200 atomic positions in the *x*-*y* plane and periodic boundary conditions were applied in the *x* and *y* directions, whereas 10 nm of vacuum was left in the *z* direction (perpendicular to sapphire substrate). Two growth centers, each containing 116 atoms with S-rich growth edges were positioned on the (0001) surface of the substrate. During the MD simulations, the volume of the simulation box was kept constant, and the Nose-Hoover thermostat was applied to control the temperature. Several bond restraints were applied to drive the set of chemical reactions that leads to W(SH)$_2$S$_2$ losing –SH groups and bonding to the growth edge. Bond restraints are an additional energy term with the harmonic form:

$$E_{\text{restraint}} = K(r - r_0)^2,$$

where *K* is the restraint coefficient, *r* is the distance between the atoms to which the restraint is applied, and r_0 is the target distance between atoms. This additional energy term drives atoms to each other to accelerate the chemical reaction that forms the targeted bond in the system. The total energy of the system that was recorded to measure the reaction barriers excluded the contribution from the bond restraint terms.

Along with other species, W(SH)$_2$S$_2$ was selected as the dominant precursor for the WS$_2$ growth

in a chamber fed with $W(CO)_6$, SH_2, and H_2 gases. In order to bind to the growth edge, this precursor should lose two –SH groups. Out of many possible chains of reactions, the WS_2 growth was modeled via the $W(SH)_2S_2$ precursor approaching the growth edge while breaking W–S bonds at the sapphire surface. The critical role played by the sapphire substrate was investigated via four different cases with different growth island separation. The separation between islands was varied from 1.6 nm to 0.2 nm in four different cases to model the merging of two centers to form the WS_2 monolayer. These four scenarios resemble possible reaction pathways that lead to the growth of the WS_2 monolayer with particular defect structures.

Acknowledgments

ORCID iDs

Danielle Reifsnyder Hickey ⬤
https://orcid.org/0000-0002-8962-1473
Mikhail Chubarov ⬤ https://orcid.org/0000-0002-4722-0321
Joan M Redwing ⬤ https://orcid.org/0000-0002-7906-452X

References

[1] Wei J W, Ma Z W, Zeng H, Wang Z Y, Wei Q and Peng P 2012 Electronic and optical properties of vacancy-doped WS_2 monolayers *AIP Adv.* **2** 042141

[2] Jeong H Y, Jin Y, Yun S J, Zhao J, Baik J, Keum D H, Lee H S and Lee Y H 2017 Heterogeneous defect domains in single-crystalline hexagonal WS_2 *Adv. Mater.* **29** 1–6

[3] Mahjouri-Samani M *et al* 2016 Tailoring vacancies far beyond intrinsic levels changes the carrier type and optical response in monolayer $MoSe_{2-x}$ crystals *Nano Lett.* **16** 5213–20

[4] Li L and Carter E A 2019 Defect-mediated charge-carrier trapping and nonradiative recombination in WSe_2 monolayers *J. Am. Chem. Soc.* **141** 10451–61

[5] Li M, Wan Y and Wang W 2017 Prediction of mechanical properties for defective monolayer MoS_2 with single molybdenum vacancy defects using molecular dynamics simulations. *2017 IEEE 17th Int. Conf. Nanotechnology, NANO 2017, No. Model I* pp 9–12

[6] Wu J, Fan Z, Chen J and Jiang X 2018 Atomic defects in monolayer WSe_2 tunneling FETs studied by systematic *ab initio* calculations *Appl. Phys. Express* **11** 0–4

[7] Komsa H P, Kotakoski J, Kurasch S, Lehtinen O, Kaiser U and Krasheninnikov A V 2012 Two-dimensional transition metal dichalcogenides under electron irradiation: defect production and doping *Phys. Rev. Lett.* **109** 1–5

[8] Komsa H P, Kurasch S, Lehtinen O, Kaiser U and Krasheninnikov A V 2013 From point to extended defects in two-dimensional MoS_2: evolution of atomic structure under electron irradiation *Phys. Rev.* B **88** 1–8

[9] Azizi A, Zou X, Ercius P, Zhang Z, Elías A L, Perea-López N, Stone G, Terrones M, Yakobson B I and Alem N 2014 Dislocation motion and grain boundary migration in two-dimensional tungsten disulphide *Nat. Commun.* **5** 4867

[10] Wang S, Do L G, Lee S, Yoon E and Warner J H 2016 Detailed atomic reconstruction of extended line defects in monolayer MoS_2 *ACS Nano* **10** 5419–30

[11] Roy S, Choi W, Jeon S, Kim D H, Kim H, Yun S J, Lee Y, Lee J, Kim Y M and Kim J 2018 Atomic observation of filling vacancies in monolayer transition metal sulfides by chemically sourced sulfur atoms *Nano Lett.* **18** 4523–30

[12] Coelho P M, Komsa H P, Coy Diaz H, Ma Y, Krasheninnikov A V and Batzill M 2018 Post-synthesis modifications of two-dimensional $MoSe_2$ or $MoTe_2$ by incorporation of excess metal atoms into the crystal structure *ACS Nano* **12** 3975–84

[13] Ji H G, Lin Y C, Nagashio K, Maruyama M, Solís-Fernández P, Sukma Aji A, Panchal V, Okada S, Suenaga K and Ago H 2018 Hydrogen-assisted epitaxial growth of monolayer tungsten disulfide and seamless grain stitching *Chem. Mater.* **30** 403–11

[14] Kang K, Xie S, Huang L, Han Y, Huang P Y, Mak K F, Kim C J, Muller D and Park J 2015 High-mobility three-atom-thick semiconducting films with wafer-scale homogeneity *Nature* **520** 656–60

[15] Gao Y *et al* 2015 Large-area synthesis of high-quality and uniform monolayer WS_2 on reusable Au foils *Nat. Commun.* **6** 8569

[16] Chiappe D *et al* 2018 Layer-controlled epitaxy of 2D semiconductors: bridging nanoscale phenomena to wafer-scale uniformity *Nanotechnology* **29** 425602

[17] Lan C, Zhou Z, Zhou Z, Li C, Shu L, Shen L, Li D, Dong R, Yip S P and Ho J C 2018 Wafer-scale synthesis of monolayer WS_2 for high-performance flexible photodetectors by enhanced chemical vapor deposition *Nano Res.* **11** 3371–84

[18] Zhang X, Choudhury T H, Chubarov M, Xiang Y, Jariwala B, Zhang F, Alem N, Wang G C, Robinson J A and Redwing J M 2018 Diffusion-controlled epitaxy of large area coalesced WSe_2 monolayers on sapphire *Nano Lett.* **18** 1049–56

[19] Chen J *et al* 2019 Synthesis of wafer-scale monolayer WS_2 crystals toward the application in integrated electronic devices *ACS Appl. Mater. Interfaces* **11** 19381–7

[20] Chubarov M *et al* 2020 Wafer-scale epitaxial growth of single orientation WS_2 monolayers on sapphire (arXiv: 2006.10952 [Cond-mat.mtrl-sci])

[21] Reifsnyder Hickey D *et al* 2020 Illuminating invisible grain boundaries in coalesced single-orientation WS_2 monolayer films (*arXiv:* 2006.11668 *[Cond-mat.mtrl-sci]*)

[22] Yang P *et al* 2020 Epitaxial growth of centimeter-scale single-crystal MoS_2 monolayer on Au(111) *ACS Nano* **14** 5036–45

[23] Zhang S, Wang C G, Li M Y, Huang D, Li L J, Ji W and Wu S 2017 Defect structure of localized excitons in a WSe_2 monolayer *Phys. Rev. Lett.* **119** 1–6

[24] Jiang X W, Gong J, Xu N, Li S S, Zhang J, Hao Y and Wang L W 2014 Enhancement of band-to-band tunneling in mono-layer transition metal dichalcogenides two-dimensional materials by vacancy defects *Appl. Phys. Lett.* **104** 023512

[25] Kaasbjerg K, Martiny J H J, Low T and Jauho A P 2017 Symmetry-forbidden intervalley scattering by atomic defects in monolayer transition-metal dichalcogenides *Phys. Rev.* B **96** 1–6

[26] Zhang C, Wang C, Yang F, Huang J K, Li L J, Yao W, Ji W and Shih C K 2019 Engineering point-defect states in monolayer WSe_2 *ACS Nano* **13** 1595–1602

[27] Liang T, Shin Y K, Cheng Y-T, Yilmaz D E, Vishnu K G, Verners O, Zou C, Phillpot S R, Sinnott S B and van Duin A C T 2013 Reactive potentials for advanced atomistic simulations *Annu. Rev. Mater. Res.* **43** 109–29

[28] van Duin A C T, Dasgupta S, Lorant F and Goddard III W A 2001 ReaxFF: a reactive force field for hydrocarbons *J. Phys. Chem.* A **105** 9396–409

[29] van Duin A C T, Strachan A, Stewman S, Zhang Q, Xu X and Goddard III W A 2003 ReaxFFSiO reactive force field for silicon and silicon oxide systems *J. Phys. Chem.* A **107** 3803–11

[30] Zhang L, Zybin S V, van Duin A C T, Dasgupta S, Goddard III W A and Kober E M 2009 Carbon cluster formation during thermal decomposition of Octahydro-1,3,5,7-Tetranitro-1,3,5,7-Tetrazocine and 1,3,5-Triamino-2,4,6-Trinitrobenzene high explosives from ReaxFF reactive molecular dynamics simulations *J. Phys. Chem.* A **113** 10619–40

[31] Han S S, Choi S-H and van Duin A C T 2010 Molecular dynamics simulations of stability of metal-organic frameworks against H2O using the ReaxFF reactive force field *Chem. Commun.* **46** 5713–5

[32] Akbarian D, Yilmaz D E, Cao Y, Ganesh P, Dabo I, Munro J, Van Ginhoven R and Van Duin A C T 2019 Understanding the influence of defects and surface chemistry on ferroelectric switching: a ReaxFF Investigation of BaTiO3 *Phys. Chem. Chem. Phys.* **21** 18240–9

[33] Kelley K P, Yilmaz D E, Collins L, Sharma Y, Lee H N, Akbarian D, van Duin A C T, Ganesh P and Vasudevan R K 2020 Thickness and strain dependence of piezoelectric coefficient in BaTiO$_3$ thin films *Phys. Rev. Mater.* **4** 024407

[34] Yilmaz D E 2015 Modeling failure mechanisms of poly(p-phenylene terephthalamide) fiber using reactive potentials *Comput. Mater. Sci.* **109** 183–93

[35] Yilmaz D E and van Duin A C T 2018 Investigating structure property relations of poly (p-phenylene terephthalamide) fibers via reactive molecular dynamics simulations *Polymer (Guildf)* **154** 172–81

[36] Kowalik M, Ashraf C, Damirchi B, Akbarian D, Rajabpour S and van Duin A C T 2019 Atomistic scale analysis of the carbonization process for C/H/O/N-based polymers with the ReaxFF reactive force field *J. Phys. Chem.* B **123** 5357–67

[37] Ostadhossein A, Rahnamoun A, Wang Y, Zhao P, Zhang S, Crespi V H and van Duin A C T 2017 ReaxFF reactive force-field study of molybdenum disulfide (MoS$_2$) *J. Phys. Chem. Lett.* **8** 631–40

[38] Yilmaz D E, Lotfi R, Ashraf C, Hong S and van Duin A C T 2018 Defect design of two-dimensional MoS2 structures by using a graphene layer and potato stamp concept *J. Phys. Chem.* C **122** 11911–7

[39] Momeni K *et al* 2020 Multiscale computational understanding and growth of 2D materials: a review *npj Comput. Mater.* **6** 22

[40] Senftle T P *et al* 2016 The ReaxFF reactive force-field: development, applications and future directions *npj Comput. Mater.* **2** 15011

[41] Grimme S 2019 Exploration of chemical compound, conformer, and reaction space with meta-dynamics simulations based on tight-binding quantum chemical calculations *J. Chem. Theory Comput.* **15** 2847–62

[42] Jing Z, Xin L and Sun H 2015 Replica exchange reactive molecular dynamics simulations of initial reactions in zeolite synthesis *Phys. Chem. Chem. Phys.* **17** 25421–8

[43] Schutte W J, De Boer J L and Jellinek F 1987 Crystal structures of tungsten disulfide and diselenide *J. Solid State Chem.* **70** 207–9

[44] Hong S and Van Duin A C T 2016 Atomistic-scale analysis of carbon coating and its effect on the oxidation of aluminum nanoparticles by ReaxFF-molecular dynamics simulations *J. Phys. Chem.* C **120** 9464–74

[45] Xuan Y *et al* 2019 Multi-scale modeling of gas-phase reactions in metal-organic chemical vapor deposition growth of WSe$_2$ *J. Cryst. Growth* **527** 125247

[46] Plimpton S 1995 Fast parallel algorithms for short-range molecular dynamics *J. Comput. Phys.* **117** 1–19

[47] Aktulga H M, Fogarty J C, Pandit S A and Grama A Y 2012 Parallel reactive molecular dynamics: numerical methods and algorithmic techniques *Parallel Comput.* **38** 245–59